

Article

PEO-Based Block Copolymer Electrolytes Containing Double Conductive Phases with Improved Mechanical and Electrochemical Properties

Ze-Kun Zhang, Shi-Peng Ding, Ze Ye, Ding-Li Xia and Jun-Ting Xu * 

State Key Laboratory of Motor Vehicle Biofuel Technology, International Research Center for X Polymers, Department of Polymer Science and Engineering, Zhejiang University, Hangzhou 310027, China

* Correspondence: xujt@zju.edu.cn

Abstract: In this work, the advanced all solid-state block copolymer electrolytes (SBCPEs) for lithium-ion batteries with double conductive phases, poly(ethylene oxide)-*b*-poly(trimethyl-*N*-((2-(dimethylamino)ethyl methacrylate)-7-propyl)-ammonium bis(trifluoromethanesulfonyl) imide) (PEO-*b*-PDM-dTFSI)/LiTFSI, were fabricated, in which the charged PDM-dTFSI block contained double quaternary ammonium cations and the PEO block was doped with LiTFSI. The disordered (DIS) and ordered lamellae (LAM) phase structures were achieved by adjusting the composition of the block copolymer and the doping ratio *r*. In addition, the presence of the hard PDM-dTFSI block and the formation of the LAM phase structure resulted in a good mechanical strength of the solid PEO-*b*-PDM-dTFSI/LiTFSI electrolyte, and it could maintain a high level of 10^4 Pa at 100 °C, which was around 10,000 times stronger than that of the PEO/LiTFSI electrolyte. Based on the good mechanical and electrochemical properties, the PEO-*b*-PDM-dTFSI/LiTFSI SBCPE exhibited excellent long-term galvanostatic cycle performance, indicating the strong ability to suppress lithium dendrites.



Citation: Zhang, Z.-K.; Ding, S.-P.; Ye, Z.; Xia, D.-L.; Xu, J.-T. PEO-Based Block Copolymer Electrolytes Containing Double Conductive Phases with Improved Mechanical and Electrochemical Properties. *Materials* **2022**, *15*, 7930. <https://doi.org/10.3390/ma15227930>

Academic Editor: Satyam Panchal

Received: 16 October 2022

Accepted: 7 November 2022

Published: 9 November 2022

Publisher's Note: MDPI stays neutral with regard to jurisdictional claims in published maps and institutional affiliations.



Copyright: © 2022 by the authors. Licensee MDPI, Basel, Switzerland. This article is an open access article distributed under the terms and conditions of the Creative Commons Attribution (CC BY) license (<https://creativecommons.org/licenses/by/4.0/>).

Keywords: block copolymer; solid electrolytes; double conductive phases; mechanical strength; electrochemical properties

1. Introduction

Lithium-ion batteries (LIBs) play an important role in modern electronic devices and vehicles, and new generation batteries providing a higher energy density need to be developed to fulfill the increasing market demand [1–3]. Lithium metal is regarded as an excellent anode candidate to offer high energy density, but it will cause some serious problems when matched with flammable liquid electrolytes such as electrolyte leakage, fire, and explosion [4,5]. The solid state electrolyte may suppress the growth of lithium dendrite to improve the safety of LIBs; in particular, polymer electrolytes have received great attention due to its chemical stability and flexibility [6–8].

The poly(ethylene oxide) (PEO)/salt hybrid is a representative polymer electrolyte due to the effective dissociation of lithium salts and the good mobility of the PEO segment [9–11]. Nevertheless, the crystallization of PEO usually results in low ionic conductivity at room temperature [12,13], and the soft PEO chains cannot offer sufficient mechanical strength to inhibit the penetration of lithium dendrites [14]. To solve this problem, solid-state block copolymer (BCP) electrolytes (SBCPEs) comprising the stiff blocks have been developed. BCP electrolytes can form various nanostructures in bulk via microphase separation such as lamellae (LAM), cylinders, spheres, and etc. [15,16], which will construct the lithium ion conducting channels and the stiff domains [17–20]. For example, the frequently reported salt-doped PEO-*b*-poly(styrene) (PEO-*b*-PS) BCPs could provide a good mechanical strength and ionic conductivity (σ), but the σ value is usually lower than that of the pure PEO/salt electrolytes [21–24]. Additionally, many PEO-based BCPs with single-ion blocks have been developed to improve the electrochemical performance of SBCPEs [25], that is, the anions

were covalently attached on the polymer chains and only the Li^+ could migrate. Indeed, this greatly enhanced the lithium ion transfer number (t_{Li^+}), however, a decreased ionic conductivity was usually encountered due to the slow motion of the single-ion polymer chains [26–28]. The ionic liquid (IL) is the good additive for BCP electrolytes to improve the σ and electrochemical stability [29–32]. Fan and Shen fabricated a series of mesogen-jacketed liquid crystalline (MJLC) BCP/lithium salt/IL ternary hybrids [33], which could maintain high ionic conductivities and storage moduli at high temperatures, while the plasticization effect of ILs on other common BCPs will be more profound compared with the rigid MJLC BCPs and will sacrifice the mechanical strength of the electrolytes [34]. Therefore, simultaneous improvement of the ionic conductivity, mechanical strength, and electrochemical performances of the SBCPEs is always a contradictory challenge.

To find a good strategy to balance the different properties of the SBCPEs, BCPs with double conductive phases were proposed in our previous work. Both the soft and rigid blocks of these BCPs can associate with the lithium ions, and the phase morphologies and properties are dependent on the salt doping ratio (r) [35–37]. It was found that the ionic conductivity and the mechanical strength were simultaneously improved in the poly(propylene monothiocarbonate)-*b*-poly(ethylene oxide) (PPMTC-*b*-PEO)/LiTFSI hybrids [38], which can be mainly attributed to the presence of the second conductive phase and the microphase-separated structure. However, at a higher doping ratio ($r = 1/3$), the storage modulus of the PEO-*b*-PPMTC/LiTFSI hybrid was seriously decreased, arising from the plasticization of LiTFSI, though the σ reached a high level of 10^{-4} S/cm at 30 °C [38]; moreover, the measurement of the electrochemical performance was hard to conduct on these viscous electrolytes with a high r because of the failure of film formation, which limits their further practical application. Therefore, it is necessary to find a better conductive rigid block for the PEO-based SBCPE to meet the test requirement of the LIBs and improve their electrochemical performances.

In recent years, the studies on the poly(ionic liquid)s (PILs)-based electrolytes have attracted much attention due to its extensive synthetic strategies [39] and excellent electrochemical stability [40]. On the other hand, the introduction of PIL blocks into BCPs can improve the phase separation strength of BCPs and induce the formation of ordered ion-conducting channels [41,42]. In PIL/salt hybrids, the transportation of Li^+ is mainly dominated by the “vehicular mechanism”, and the polycations can also interact with the anions from lithium salts [7,43]. In this case, the lithium ion transfer number and electrochemical stability of the PIL/salt electrolytes were improved [44,45], and the t_{Li^+} was higher for the PILs with multiple cations [46]. With the consideration of the excellent electrochemical stability of PILs and the good conductivity and mechanical strength of double conductive phases, in this work, the novel poly(trimethyl-*N*-((2-(dimethylamino)ethyl methacrylate)-7-propyl)-ammonium bis(trifluoromethanesulfonyl) imide) (PDM-dTFSI) block with double quaternary ammonium cations was introduced into the PEO-*b*-PDM-dTFSI BCPs as one of the conductive phases for the first time. The relative rigid PDM-dTFSI block can not only provide mechanical strength but also contribute to ionic conductivity as a second conductive phase, which is expected to simultaneously improve the mechanical strength and electrochemical performances of the SBCPEs. The effects of the BCP composition and salt doping ratio on the phase-separated structures and ionic conductivities of the PEO-*b*-PDM-dTFSI/LiTFSI SBCPEs were systematically investigated. The SBCPE with the optimal ionic conductivity was chosen to proceed with further electrochemical measurements, demonstrating the good film-forming capacity and stable long-term lithium stripping and plating performance. This work provides an efficient idea to trade-off the ionic conductivity, mechanical strength, and electrochemical performance of SBCPEs.

2. Materials and Methods

2.1. Materials

2-(Dimethylamino)ethyl methacrylate (DM, 99%), 2-bromoisobutryl bromide (98%), and 1,1,4,7,10,10-hexamethyltriethylenetetramine (HMTTA) were purchased from Aladdin. Polyethy-

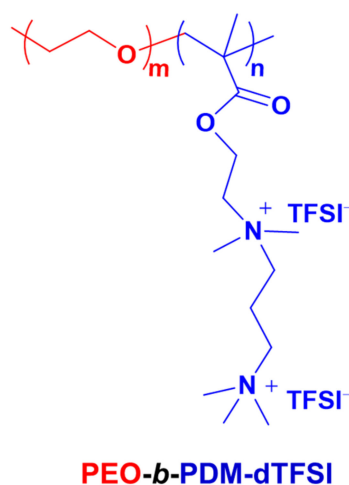
lene glycol monomethyl ether (PEO, $M_n = 5000$ g/mol) and (3-bromopropyl)trimethylammonium bromide (97%) were obtained from TCI. PEO and DM monomers were washed with basic alumina to remove the polymerization inhibitors prior to use. Tetrahydrofuran (THF) from Sinopharm Chemicals was refluxed with sodium hydride. Super dry dimethylformamide (DMF) and bis(trifluoromethane) sulfonimide lithium (LiTFSI, 98%) from J&K Scientific were used as received. Li metal anode (diameter = 12 mm) was obtained from China Energy Lithium Co., Ltd., Tianjin, China.

2.2. Synthesis of PEO-*b*-PDM BCPs

PEO-*b*-PDM BCPs were synthesized by atom transfer radical polymerization (ATRP). First, the PEO-Br macroinitiator was prepared by esterification of PEO with 2-bromoisobutyryl bromide. Then, a series of PEO-*b*-PDM_{*n*} BCPs were obtained through conducting the ATRP polymerization of DM, where the subscription *n* represents the polymerization degree of the PDM block. The specific experimental process and characterization results of PEO-*b*-PDM BCPs can be found in the Supplementary Materials.

2.3. Synthesis of PEO-*b*-PDM-*d*TFSI Charged BCPs

First, the PDM block of PEO-*b*-PDM_{*n*} BCPs was quaternized with (3-bromopropyl)trimethylammonium bromide to give the PEO-*b*-PDM_{*n*}-*d*Br intermediate, then the target products of PEO-*b*-PDM_{*n*}-*d*TFSI BCPs were obtained by the ionic exchange reaction of PEO-*b*-PDM_{*n*}-*d*Br against LiTFSI in DMF. The detailed process is described in the Supplementary Materials, and the structure and the molecular characteristics of PEO-*b*-PDM-*d*TFSI BCP are illustrated in Scheme 1 and Table 1, respectively.



Scheme 1. Structure of the PEO-*b*-PDM-*d*TFSI BCP.

Table 1. Molecular characteristics of the PEO₁₁₄-*b*-PDM_{*n*}-*d*TFSI samples.

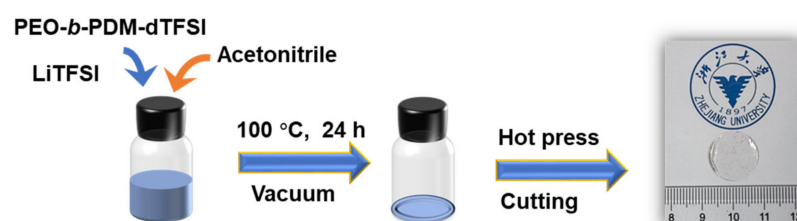
Samples	M_n^a (g/mol)	D^b	f_{PEO}^c (%)
PEO ₁₁₄ - <i>b</i> -PDM ₁₅ - <i>d</i> TFSI	17,200	1.24	33.9
PEO ₁₁₄ - <i>b</i> -PDM ₃₆ - <i>d</i> TFSI	34,400	1.21	17.6
PEO ₁₁₄ - <i>b</i> -PDM ₅₅ - <i>d</i> TFSI	49,900	1.19	12.3

^a Number-average molecular weight, obtained by ¹H-NMR spectra. ^b $D = M_w/M_n$, dispersity for the uncharged sample tested by GPC. ^c Volume fraction of PEO, calculated according to the densities of PEO and PDM-*d*TFSI (Table S2).

2.4. Fabrication of Solid-State Block Copolymer Electrolytes

A certain amount of acetonitrile solution of PEO-*b*-PDM_{*n*} and LiTFSI salt was mixed and stirred for 12 h to blend homogeneously. The above solution was first placed under

dynamic vacuum for 8 h at room temperature and then evacuated in a vacuum oven at 100 °C for 24 h to completely remove the solvent. Finally, the obtained solid electrolytes were stored in the glove box filled with nitrogen (the content of O₂ and H₂O is less than 0.1 ppm) and named as PEO-*b*-PDM_{*n*}-dTFPI-*r*, where *r* is the molar ratio of LiTFSI to the sum of EO units and N cation (i.e., [Li⁺]/([EO]+[N⁺])). The solid electrolyte used for the assembling cell was hot-pressed into a film with a thickness of 100 μm at 40 °C and then cut into a circular film with a diameter of 16 mm (Scheme 2).



Scheme 2. Schematic illustration of the fabrication of SBCPEs.

2.5. Battery Assembly

All cells including Li/Li symmetric cells and Li/stainless steel (SS) cells were assembled in the glove box filled with argon. The edges of the electrolyte will become slightly thicker after being cut into round films, which may result in the non-uniform contact between the electrolyte film and the electrode. Therefore, before testing, the cells were heated under 60 °C for 24 h to achieve good contact between the electrodes and the solid polymer electrolyte.

2.6. Characterizations

The composition and number-averaged molecular weight (M_n) of the samples were calculated according to the ¹H-NMR spectra recorded on a Bruker DMX-400 instrument (400 MHz). The polydispersity indices of PEO-*b*-PDM_{*n*} BCPs were measured by gel permeation chromatography (GPC) on a Waters system instrument using DMF containing 0.05 M LiBr as the mobile phase with a leaching rate of 1 mL/min at 40 °C, calibrated by the polystyrene standards. Differential scanning calorimetry (DSC) characterization was conducted on a TA DSC 25 instrument. About 5 mg of the sample was sealed in an aluminum pan, and the first cooling and second heating curves at the ramp rates of 20 °C/min were plotted. Small-angle X-ray scattering (SAXS) measurement was performed on the BL16B1 beamline of the Shanghai Synchrotron Radiation Facility (SSRF) equipped with a Pilatus 2M detector. The energy of the incident X-ray was 10 keV and the distance from the sample to detector was 1940 mm. All of the samples were annealed at 100 °C under dynamic vacuum for 24 h and then naturally cooled down to room temperature. The samples for temperature-variable tests were heated from 30 to 100 °C at a rate of 10 °C/min. Before data collection, the sample was held at the target temperature for about 3 min to achieve thermal equilibrium. The raw two-dimensional patterns were transformed into one-dimensional data using the Fit 2D tool, and the scattering vector (q) of the SAXS profiles was calibrated with silver behenate. Rheological tests were carried out on a HAAKE MARS 60 rheometer using 20 mm diameter parallel plates, and the gap thickness was 1 mm. A fixed strain amplitude (1%) was used, and the temperature sweep data with a frequency of 1 Hz between 30 and 100 °C were collected upon heating with a heating rate of 2 °C/min. During the tests, the polymer electrolyte may inevitably absorb trace amounts of water, resulting in slightly lower mechanical strength than the true value. The temperature-variable ionic conductivity (σ) of the solid polymer electrolyte film was measured on a CHI660E electrochemical workstation equipped with a Linkam hot stage at a frequency range from 1 MHz to 1 Hz. The electrolyte films were sandwiched between two stainless steel electrodes. The bulk resistance (R) was determined by extrapolating the high-frequency plateau value of the real part impedance. The σ was obtained via

the equation $\sigma = L/(SR)$, where L and S are the thickness and area of the electrolyte film, respectively. The thicknesses of the electrolytes used for the conductivity measurements are 1 mm. The average conductivity was taken from the three parallel tests. The lithium ion transference number (t_{Li^+}) was obtained on the CHI660E electrochemical workstation at 30 °C by assembling Li/Li symmetric cells. t_{Li^+} is calculated by the equation: $t_{\text{Li}^+} = [I_s(\Delta V - I_0 R_0)]/[I_0(\Delta V - I_s R_s)]$, where ΔV is the applied polarization voltage of 10 mV, I_0 and I_s are the initial and the steady-state current measured by DC polarization, respectively. R_0 and R_s represent the interfacial resistance before and after polarization obtained from the AC impedance spectrum, respectively. Linear sweep voltammetry (LSV) was also conducted on the CHI660E electrochemical workstation. The Li/SS cell with stainless steel as the working electrode and Li metal as the counter electrode was assembled. The cut-off voltage and sweep rate were 6 V and 1 mV/s, respectively. The constant current cycling performance of the Li/Li symmetrical cells was performed on the LAND device with the current densities of 0.05 mA/cm² and 0.1 mA/cm² at 60 °C.

3. Results and Discussion

3.1. Thermal and Phase Behavior of the PEO-*b*-PDM-*d*TFSI/LiTFSI Electrolytes

The crystallization behavior and glass transition temperature (T_g) of the PEO₁₁₄-*b*-PDM_{*n*}-*d*TFSI/LiTFSI hybrids were determined by DSC. As shown in Figure 1a, a distinct endothermic peak was observed in PEO₁₁₄-*b*-PDM₁₅-*d*TFSI, representing the melting peak of the PEO block ($T_m = 49.7$ °C), and this peak disappeared in the salt-doped PEO₁₁₄-*b*-PDM₁₅ hybrids, which can be attributed to the suppression of the PEO crystallization after the lithium ions complex with the PEO chains. In addition, all the PEO₁₁₄-*b*-PDM₁₅-*d*TFSI/LiTFSI hybrids exhibited two glass transition steps, indicating the occurrence of the phase separation between these two blocks. For instance, the double T_g s of the PEO₁₁₄-*b*-PDM₁₅-*d*TFSI-1/10 hybrids were assigned to the PEO ($T_g^{\text{PEO}} = -36.8$ °C) and PDM-*d*TFSI ($T_g^{\text{PDM-dTFSI}} = 74.2$ °C) blocks, respectively. With the increase in the doping ratio r , the T_g^{PEO} increased while $T_g^{\text{PDM-dTFSI}}$ decreased (Figure 1a and Table 2). The increased T_g^{PEO} was ascribed to the higher number of associating points between the Li⁺ and EO units, lowering the mobility of PEO segments [47]. In contrast, the gradual decrease in $T_g^{\text{PDM-dTFSI}}$ resulted from a disruption of the aggregation between the charged PDM-*d*TFSI chains and the TFSI⁻ in the presence of LiTFSI. The significant drop in T_g with the increase in the salt content has also been reported in the PIL/salt hybrids [44]. When the polymerization degree of the PDM-*d*TFSI block is increased to 36, one can see only one T_g at ~11.5 °C for the salt-absent sample. However, the DSC curves of the PEO₁₁₄-*b*-PDM₃₆-*d*TFSI-*r* hybrids contained two separated T_g s at $r = 1/10$ and $1/5$, and then re-back to only one T_g at a higher doping ratio ($r = 1/3$), reflecting the complicated change in the phase separation state with r in PEO₁₁₄-*b*-PDM₃₆-*d*TFSI/LiTFSI hybrids. Therefore, the obtained PEO₁₁₄-*b*-PDM_{*n*}-*d*TFSI-*r* electrolytes possessed the soft (PEO) and relatively hard (PDM-*d*TFSI) block, and the crystallization of the PEO block could be fully suppressed by adjusting the composition and the doping ratio. On the other hand, the phase separation behavior of the salt-doped PEO₁₁₄-*b*-PDM_{*n*}-*d*TFSI was considered to be relevant with the salt content, which will be confirmed by the SAXS results.

The phase behavior of the PEO-*b*-PDM-*d*TFSI BCPs was studied first. The SAXS profiles of the PEO₁₁₄-*b*-PDM_{*n*}-*d*TFSI BCPs with different PDM-*d*TFSI block lengths are shown in Figure S5. The scattering peaks with the vector ratio of 1:2 was observed when $n = 15$, implying the formation of a LAM structure. When the PDM-*d*TFSI content increased ($n = 36$ and 55), the LAM structure disappeared and was replaced by the compatible state, as revealed by the absence of the primary scattering peaks (Figure S5). This is because the f_{PEO} is decreased with the increase in the polymerization degree of the PDM-*d*TFSI block (Table 1), which will decrease the phase separation ability between two blocks.

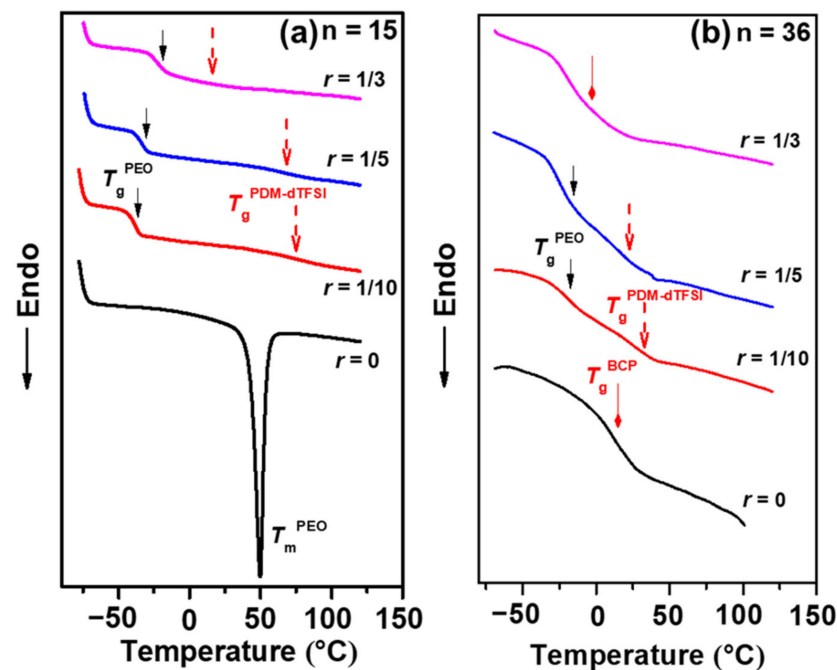


Figure 1. The DSC curves of the PEO₁₁₄-*b*-PDM_{*n*}-dTFSI/LiTFSI electrolytes when *n* is (a) 15 and (b) 36 in the second heating scans.

Table 2. Thermal properties of the PEO₁₁₄-*b*-PDM_{*n*}-dTFSI/LiTFSI hybrids.

Samples	$f_{\text{PEO/LiTFSI}}^a$ (%)	T_g^{PEO} (°C)	$T_g^{\text{PDM-dTFSI}}$ (°C)	T_m^{PEO} (°C)
PEO ₁₁₄ - <i>b</i> -PDM ₁₅ -dTFSI	33.9	n/a	n/a	49.7
PEO ₁₁₄ - <i>b</i> -PDM ₁₅ -dTFSI-1/10	40.3	−36.8	74.2	n/a
PEO ₁₁₄ - <i>b</i> -PDM ₁₅ -dTFSI-1/5	45.3	−31.7	67.1	n/a
PEO ₁₁₄ - <i>b</i> -PDM ₁₅ -dTFSI-1/3	50.6	−19.3	15.7	n/a
PEO ₁₁₄ - <i>b</i> -PDM ₃₆ -dTFSI	17.6		11.5	n/a
PEO ₁₁₄ - <i>b</i> -PDM ₃₆ -dTFSI-1/10	21.9	−19.8	33.5	n/a
PEO ₁₁₄ - <i>b</i> -PDM ₃₆ -dTFSI-1/5	25.7	−15.1	23.3	n/a
PEO ₁₁₄ - <i>b</i> -PDM ₃₆ -dTFSI-1/3	29.9		−3.9	n/a

^a Volume fraction of the PEO/LiTFSI hybrid, calculated according to the densities of the PEO/LiTFSI and PDM-dTFSI/LiTFSI blocks (Table S2).

After doping with salts, the phase behavior of the PEO-*b*-PDM-dTFSI/LiTFSI electrolytes was different from that of the undoped BCPs, which varied with the doping ratio *r*. As shown in Figure 2a, the ordered LAM structure remained in the PEO₁₁₄-*b*-PDM₁₅-dTFSI/LiTFSI hybrid with *r* = 1/10, while the phase structure became less ordered with the increasing doping ratio, as confirmed by the broader first-order peaks at *r* = 1/5 and 1/3 (Figure 2a). As for the PEO₁₁₄-*b*-PDM₃₆-dTFSI/LiTFSI electrolytes, only one primary peak could be observed when the salt ratio was 1/10, indicating the occurrence of the disordered phase structure induced by salt doping (Figure 2b). In contrast, the scattering peaks were unobvious and almost disappeared when *r* was increased to 1/5 and 1/3, implying that the phase separation tendency was weakened at higher doping ratios, which was similar to that of the PEO₁₁₄-*b*-PDM₁₅-dTFSI/LiTFSI hybrids. The increased compatibility between two blocks was also in accordance with the DSC results (Figure 1b), where the glass transitions of two phases can hardly be distinguished at *r* = 1/3. In the PEO-*b*-PDM-dTFSI/LiTFSI electrolyte, the LiTFSI can be dissolved into the PEO phase due to the complexation between the Li⁺ and -C-O-C- group of the PEO chains [48]. Meanwhile, the quaternary ammonium cations and TFSI anions of the charged PDM-dTFSI block had

the ability to electrostatically associate with the TFSI[−] and Li⁺, respectively [43], so that the lithium salts also existed in the PDM-dTFSI domain, especially at high salt contents. When salts were located in both phases, the electrostatic interaction between these two blocks was resultantly produced, and the attraction will be increased and become more remarkable with the increase in r . This is why the enhanced compatibility between two blocks was observed at higher doping ratios (Figure 2). The above results indicate that the ordered LAM or disordered structure can be achieved in PEO₁₁₄-*b*-PDM _{n} -dTFSI/LiTFSI electrolytes by adjusting the length of the charged block and the doping ratio r . Since both phases carry charges, double ion-channels are provided for the transport of lithium ions. On the other hand, the ordered LAM structure endows the solid electrolyte film with good mechanical properties, which will be examined in the following part.

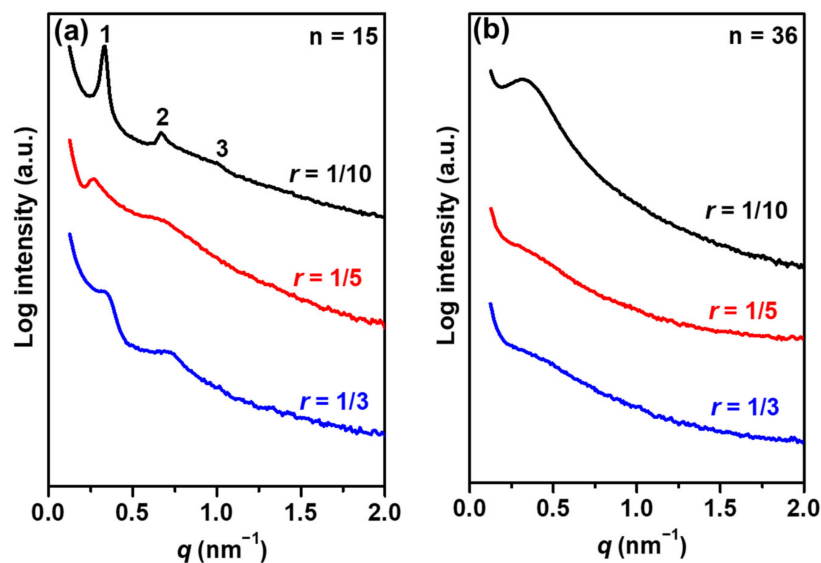


Figure 2. SAXS profiles of the PEO₁₁₄-*b*-PDM _{n} -dTFSI/LiTFSI electrolytes with different doping ratios at 30 °C when (a) $n = 15$ and (b) 36.

3.2. Mechanical Properties of the PEO-*b*-PDM-dTFSI/LiTFSI Electrolytes

The mechanical properties of the solid electrolyte films were investigated by the temperature-variable rheological tests. As for the PEO₁₁₄-*b*-PDM₁₅-dTFSI/LiTFSI electrolytes (Figure 3a), the storage modulus (G') of the salt-absent sample was around 10^5 Pa at 30 °C, but suddenly dropped to 10^3 Pa during 45–60 °C due to melting of the PEO block (Figure 1a). When the salt doping ratio r was increased to 1/10 and 1/5, the G' maintained the level of 10^5 Pa at room temperature and changed moderately with the increase in temperature, and was still higher than 10^4 and 10^3 Pa at 100 °C, respectively. Specifically, the mechanical properties of the electrolyte at $r = 1/10$ exhibited an excellent temperature stability (Figure 3a). This is because the high ordered and thermally stable LAM structure is formed in the PEO₁₁₄-*b*-PDM₁₅-dTFSI-1/10 hybrid (Figure S6). It should be noted that the mechanical properties of the PEO₁₁₄-*b*-PDM₁₅-dTFSI/LiTFSI hybrids was far better than that of the typical PEO/salt electrolytes (below 10 Pa at the molten state) [38], which will enhance the ability to resist lithium dendrite and improve the cycle performance of the lithium-ion battery. In order to confirm the influence of the phase separation on the mechanical strength of the BCP electrolyte, the moduli of the PEO₁₁₄-*b*-PDM₃₆-dTFSI/LiTFSI hybrids were further studied. Theoretically, the G' of the PEO₁₁₄-*b*-PDM _{n} -dTFSI/LiTFSI with $n = 36$ should be better than that of $n = 15$ due to its higher content of the rigid PDM-dTFSI block. Nevertheless, the temperature-variable rheological experiment showed that the storage moduli of the PEO₁₁₄-*b*-PDM₃₆-dTFSI/LiTFSI hybrids decreased rapidly with the increase in temperature and was only ~100 Pa at 100 °C when $r \leq 1/5$ (Figure 3b). The relatively poor mechanical property can be attributed to the weak and disordered

phase structure of the PEO₁₁₄-*b*-PDM₃₆-dTFSI/LiTFSI BCPs (Figure 2b). In our previous studies, the mechanical strength improvements were also achieved in the phase separated BCP electrolyte compared to the BCPs with a homogenous state [38]. At the high doping ratio ($r = 1/3$), both the PEO₁₁₄-*b*-PDM_{*n*}-dTFSI/LiTFSI ($n = 36$ and 15) electrolytes exhibited lower moduli than the hybrids with $r = 1/10$ and $r = 1/5$ (Figure 3), which is probably due to the plasticization of lithium salts to the BCPs together with the weaker phase separation ability of the electrolyte at the high salt content.

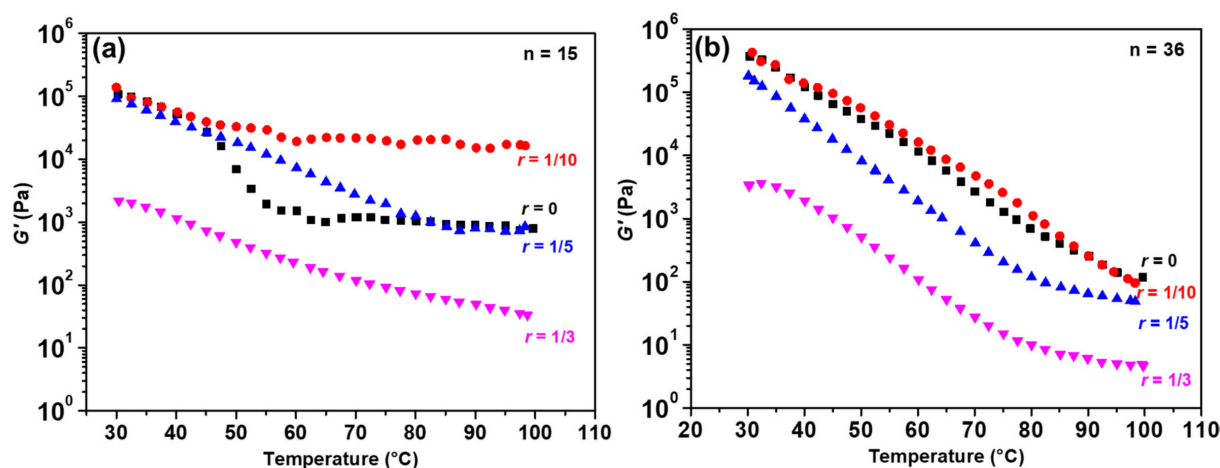


Figure 3. Storage moduli (G') of the PEO₁₁₄-*b*-PDM_{*n*}-dTFSI/LiTFSI electrolytes with different doping ratios upon heating when (a) $n = 15$ and (b) 36.

3.3. Electrochemical Properties of the PEO-*b*-PDM-dTFSI/LiTFSI Electrolytes

First, the ionic conductivity of the PEO₁₁₄-*b*-PDM_{*n*}-dTFSI/LiTFSI hybrids with various r_s was studied. As shown in Figure 4a, the similar changing trend of ionic conductivity was observed for all three samples with different PDM-dTFSI block lengths, that is, the ionic conductivity increased first and then decreased as the doping ratio r rose. On the other hand, it was found that the PEO₁₁₄-*b*-PDM₁₅-dTFSI sample possessed the highest ionic conductivity among these three BCPs, and the doping ratio for achieving its optimal σ in our experimental doping range was 1/5. In the commonly studied PEO/LiTFSI and PEO-*b*-PS/LiTFSI electrolytes, the r was $\sim 1/12$ when the conductivity was maximized [49], which was much lower than that of the PEO₁₁₄-*b*-PDM_{*n*}-dTFSI BCPs. The PDM-dTFSI blocks with double cationic groups could also dissolve the lithium salts, which will alleviate the aggregation of lithium salts and increase the number of “free” charge carriers. Therefore, the PEO₁₁₄-*b*-PDM_{*n*}-dTFSI BCPs achieved the maximal σ at a larger r . A similar situation has also been reported in some PEO-*b*-poly(zwitterion)/salt hybrids [50]. On the other hand, it was found that the ionic conductivity of the electrolytes increased with the decreasing n , and the highest σ reached the order of 10^{-5} S/cm in the PEO₁₁₄-*b*-PDM₁₅-dTFSI-1/5 hybrid at 30 °C. As for the PEO₁₁₄-*b*-PDM_{*n*}-dTFSI/LiTFSI hybrids, the PEO block was the major conductive phase, which is mainly responsible for transporting ions, so a higher σ value was obtained in the BCPs with a larger volume fraction of the PEO block (Table 1). Furthermore, the temperature-variable conductivity was measured for the PEO₁₁₄-*b*-PDM₁₅-dTFSI/LiTFSI hybrids at $r = 1/10$, 1/5, and 1/3. It can be seen from Figure 4b that the ionic conductivity at different r s increased with a temperature rise in the range of 30–100 °C, and the σ values at the optimal ratio ($r = 1/5$) were 1.6×10^{-5} and 1.1×10^{-4} S/cm at 30 °C and 60 °C, respectively, which are comparable to most solid polymer electrolytes [51–53] and are able to meet the requirement for lithium ion cells. In addition, the conductivity–temperature curve was fitted using the Vogel-Tammann-Fulcher (VTF) equation [54] to calculate the activation energy (E_a) of the PEO₁₁₄-*b*-PDM₁₅-dTFSI/LiTFSI hybrids. It was found that the data at different salt doping ratios followed the VTF equation well in the experimental temperature range, and the E_a values were 8.72, 8.39, and 8.48 kJ/mol at

$r = 1/10, 1/5,$ and $1/3,$ respectively (Table S3), indicating the lowest energy barrier for the transportation of lithium ions at $r = 1/5.$

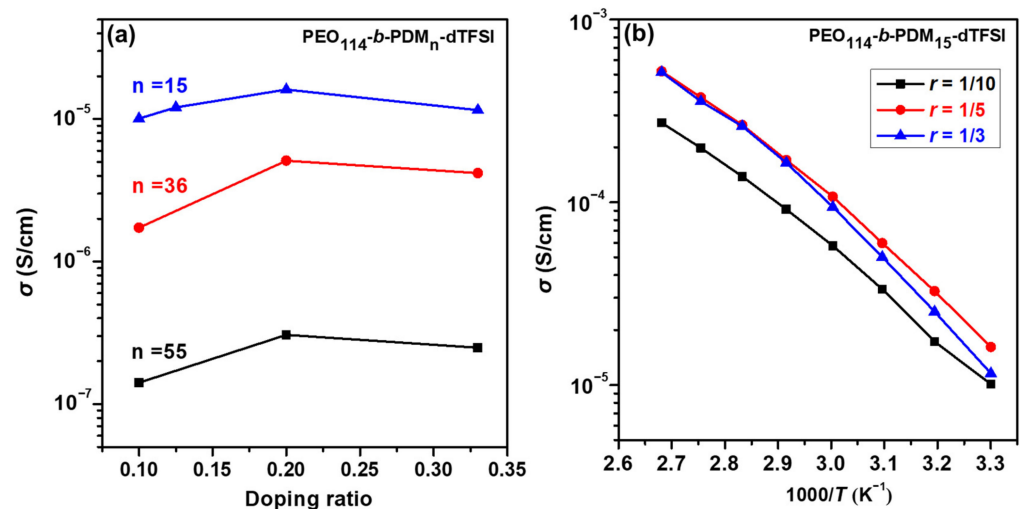


Figure 4. (a) Ionic conductivity of the PEO₁₁₄-*b*-PDM_{*n*}-dTFESI/LiTFSI hybrids at 30 °C. (b) Temperature dependence of ionic conductivity of PEO₁₁₄-*b*-PDM₁₅-dTFESI/LiTFSI hybrids with different doping ratios.

The PEO₁₁₄-*b*-PDM₁₅-dTFESI-1/5 electrolyte with the highest ionic conductivity was selected to further investigate other electrochemical properties. The t_{Li^+} represents the migrating characteristic of lithium ions in the solid electrolytes. A large t_{Li^+} value can alleviate the concentration polarization and reduce dendrite nucleation [6]. The t_{Li^+} was determined by the chronoamperometric current and the impedance spectra before and after polarization (Figure 5). The calculated t_{Li^+} value was 0.247 for the PEO₁₁₄-*b*-PDM₁₅-dTFESI-1/5 hybrid at 30 °C, which was slightly higher than that of the traditional PEO-based BCPs and brush polymer electrolytes [55–57]. A relative higher lithium ion transfer number was also achieved in some PIL/salt electrolytes compared to the neutral polymer/salt hybrid [45], and the improvement was more profound when the PILs contained multiple cations [46]. Additionally, a slightly higher t_{Li^+} of 0.255 was observed in the PEO₁₁₄-*b*-PDM₃₆-dTFESI-1/5 electrolyte containing more composition of the PDM-dTFESI block (Figure S7) compared with the PEO₁₁₄-*b*-PDM₁₅-dTFESI-1/5 electrolyte. This demonstrates that the introduction of the di-cationic groups into BCPs is indeed an effective strategy to enhance t_{Li^+} . Due to the attractive interaction between the double quaternary ammonium cations of the charged PDM-dTFESI block and the TFSI[−] anions, the movement of TFSI[−] will be restricted to some extent, making for the easier migration of Li⁺.

The electrochemical stability window of the PEO₁₁₄-*b*-PDM₁₅-dTFESI-1/5 hybrid was tested by the linear sweep voltage (LSV) at a scan rate of 1 mV/s. An oxidative decomposition voltage of ~4.28 V was observed for the PEO₁₁₄-*b*-PDM₁₅-dTFESI-1/5 hybrid (Figure 6), which was larger than the 3.8 V of the PEO/LiTFSI electrolyte [58]. This shows that the PEO₁₁₄-*b*-PDM₁₅-dTFESI-1/5 could satisfy the operation voltage when applied in Li/lithium iron phosphate (LFP) batteries.

The long-term cycle property is one of the most critical indicators to measure the quality of lithium metal batteries, which represents the stability of the interface between the solid electrolyte and the electrode and the ability to inhibit lithium dendrites [59]. Therefore, galvanostatic Li plating and stripping experiments were performed on the Li/PEO₁₁₄-*b*-PDM₁₅-dTFESI-1/5/Li symmetric cell to investigate the cycling stability. Initially, the Li/PEO₁₁₄-*b*-PDM₁₅-dTFESI-1/5/Li cell was charged and discharged, respectively, for 1 h with the current density of 0.05 mA/cm² at 60 °C for each cycle. As shown in Figure 7a, the symmetric cell containing the PEO₁₁₄-*b*-PDM₁₅-dTFESI-1/5 electrolyte had a small polarization voltage (~0.28 V) and no short circuit occurred after stable cycling for even 1000 h.

Then, the current density was increased to 0.1 mA/cm^2 and then suddenly decreased to 0.05 mA/cm^2 , proceeding 100 h under these two conditions, respectively. After cycling under the alternative current, the polarization voltage of the cell could still return to a stable plateau of $\sim 0.27 \text{ V}$. This indicates that the solid $\text{PEO}_{114}\text{-}b\text{-PDM}_{15}\text{-dTFSI-1/5}$ electrolyte considerably promoted the stable and homogenous lithium stripping/plating behavior and effectively restrained the lithium dendrite during cycling, which can be attributed to the good mechanical strength of the $\text{PEO}_{114}\text{-}b\text{-PDM}_{15}\text{-dTFSI-1/5}$ electrolyte (Figure 3a). As a comparison, we also investigated the cycling performance of the symmetric cell with the PEO/LiTFSI hybrid. It was found that the polarization voltage became irregular after cycling for 75 h and the short circuit suddenly emerged at 100 h (Figure 7b), which was similar to the phenomena reported by other groups [60], implying the non-uniform lithium deposition and poor mechanical properties of the PEO/LiTFSI electrolyte.

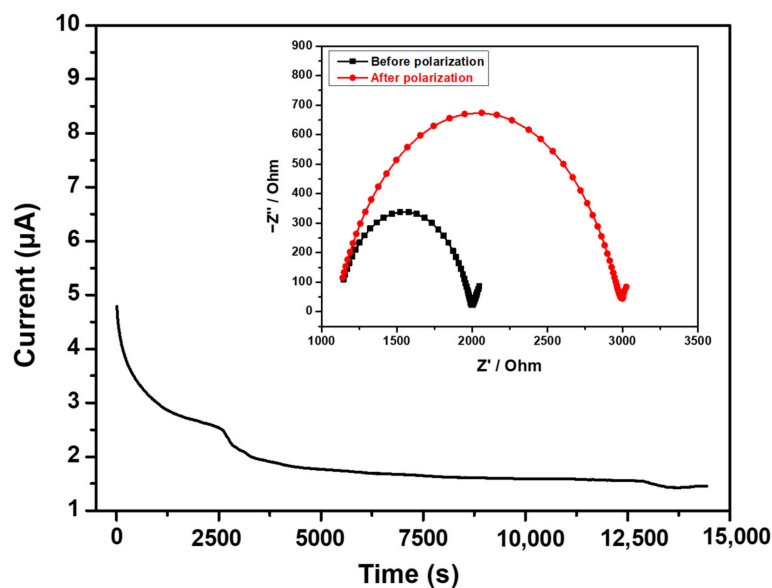


Figure 5. Chronoamperometry of the $\text{Li/PEO}_{114}\text{-}b\text{-PDM}_{15}\text{-dTFSI-1/5/Li}$ cell. The inset presents the electrochemical impedance spectroscopy (EIS) before and after polarization.

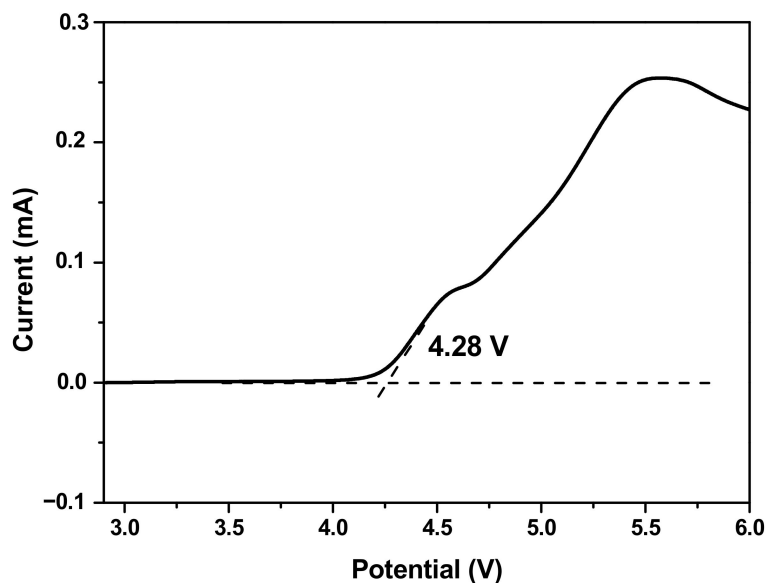


Figure 6. Linear sweep voltammetry (LSV) curve at a scan rate of 1 mV/s for the $\text{PEO}_{114}\text{-}b\text{-PDM}_{15}\text{-dTFSI-1/5}$ at $60 \text{ }^\circ\text{C}$.

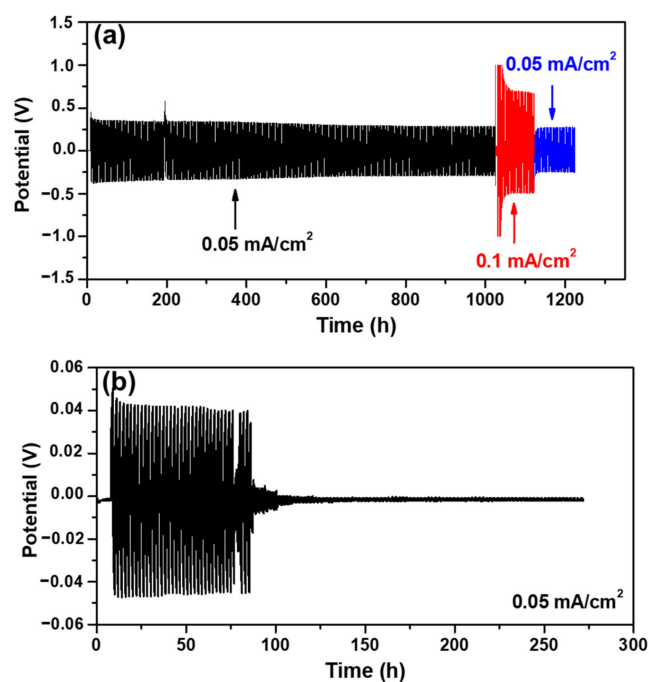


Figure 7. Galvanostatic cycling profiles for the Li | Li symmetrical cell with (a) PEO-*b*-PDM₁₅-dTFSI-1/5 and (b) PEO/LiTFSI-1/5 electrolytes at 60 °C.

Therefore, due to the existence of the double conductive phases and the thermally stable ordered phase structure, the solid PEO₁₁₄-*b*-PDM-dTFSI/LiTFSI electrolytes possess good ionic conductivity, Li⁺ mobility, and good mechanical strength in a wide temperature range, leading to a considerable improvement of the long-term cycling performance.

4. Conclusions

In conclusion, the LiTFSI-doped SBCPE with the amorphous PEO block and the charged PDM-dTFSI block were successfully developed. The PEO₁₁₄-*b*-PDM_{*n*}-dTFSI/LiTFSI electrolytes could be phase-separated into the DIS and LAM structure, depending on the composition of the BCP and doping ratio *r*. The rheology results revealed that the mechanical strength of the electrolytes was obviously enhanced due to the presence of the hard PDM-dTFSI block and the formation of the ordered and temperature-stable LAM structure, which was around 10⁴ times higher than that of the PEO/LiTFSI hybrid. In addition, LiTFSI was located in both the PEO and PDM-dTFSI domains, constructing a dual-conducting channel. After optimizing the composition and salt content, the ionic conductivity of the PEO₁₁₄-*b*-PDM₁₅-dTFSI-1/5 electrolyte with a LAM structure reached a comparably good value of 1.1 × 10⁻⁴ S/cm at 60 °C. This alleviates the problem of simultaneous improvement in the conductivity and mechanical strength of the solid BCP electrolyte. On the other hand, the double quaternary ammonium cations of the PDM-dTFSI block can interact with the TFSI anions, thereby accelerating the Li⁺ migration. In combination with the good mechanical and electrochemical properties, the assembled symmetric Li/PEO₁₁₄-*b*-PDM₁₅-dTFSI-1/5/Li cell can smoothly proceed for more than 1000 h, implying the stable interface between the solid electrolyte and the electrode. Therefore, this work demonstrates that the BCP electrolytes with both soft and relative rigid double conductive phases may offer new ideas for designing advanced SBCPEs used in lithium-ion batteries, for instance, taking PEO as a constituent block, we only need to explore other rigid conductive blocks that have good electrochemical properties and are incompatible with the PEO block.

Supplementary Materials: The following supporting information can be downloaded at: <https://www.mdpi.com/article/10.3390/ma15227930/s1>, Figures S1, S3 and S4: ¹H-NMR spectra of PEO₁₁₄-*b*-PDM_{*n*}, PEO₁₁₄-*b*-PDM_{*n*}-dBr and PEO₁₁₄-*b*-PDM_{*n*}-dTFSI; Figure S2: GPC traces of PEO₁₁₄-*b*-PDM_{*n*};

Figures S5 and S6: SAXS profiles; Figure S7: Chronoamperometry and EIS of the Li/PEO₁₁₄-*b*-PDM₃₆-dTFSI-1/5/Li cell; Scheme S1: Synthetic routes of PEO₁₁₄-*b*-PDM_{*n*} and PEO₁₁₄-*b*-PDM_{*n*}-dTFSI; Table S1: Molecular characteristics of PEO₁₁₄-*b*-PDM_{*n*}; Table S2: Densities of PEO/LiTFSI and PDM-dTFSI/LiTFSI hybrids; Table S3: Vogel-Tammann-Fulcher (VTF) equation fitting results; Ref. [61] can be found in Supplementary Materials.

Author Contributions: Conceptualization, Z.-K.Z. and J.-T.X.; Data curation, Z.-K.Z., S.-P.D., Z.Y. and D.-L.X.; Funding acquisition, J.-T.X.; Project administration, J.-T.X.; Supervision, J.-T.X.; Writing—original draft, Z.-K.Z.; Writing—review & editing, S.-P.D., Z.Y. and D.-L.X. All authors have read and agreed to the published version of the manuscript.

Funding: This research was funded by National Natural Science Foundation of China, grant number [22073082].

Institutional Review Board Statement: Not applicable.

Informed Consent Statement: Not applicable.

Data Availability Statement: Data is contained within the article and Supplementary Materials.

Conflicts of Interest: The authors declare no conflict of interest.

References

1. Yue, L.P.; Ma, J.; Zhang, J.J.; Zhao, J.W.; Dong, S.M.; Liu, Z.H.; Cui, G.L.; Chen, L.Q. All Solid-State Polymer Electrolytes for High-Performance Lithium Ion Batteries. *Energy Storage Mater.* **2016**, *5*, 139–164.
2. Piglowska, M.; Kurc, B.; Galinski, M.; Fuc, P.; Kaminska, M.; Szymlet, N.; Daszkiewicz, P. Challenges for Safe Electrolytes Applied in Lithium-Ion Cells—A Review. *Materials* **2021**, *14*, 6783–6834.
3. Zhang, Z.J.; Zhang, P.; Liu, Z.J.; Du, B.Y.; Peng, Z.Q. A Novel Zwitterionic Ionic Liquid-Based Electrolyte for More Efficient and Safer Lithium-Sulfur Batteries. *ACS Appl. Mater. Interfaces* **2020**, *12*, 11635–11642.
4. Qiu, J.L.; Liu, X.Y.; Chen, R.S.; Li, Q.H.; Wang, Y.; Chen, P.H.; Gan, L.Y.; Lee, S.J.; Nordlund, D.; Liu, Y.J.; et al. Enabling Stable Cycling of 4.2 V High-Voltage All-Solid-State Batteries with PEO-Based Solid Electrolyte. *Adv. Funct. Mater.* **2020**, *30*, 1909392.
5. Guan, Z.L.; Zhang, Z.J.; Du, B.Y.; Peng, Z.Q. A Non-Flammable Zwitterionic Ionic Liquid/Ethylene Carbonate Mixed Electrolyte for Lithium-Ion Battery with Enhanced Safety. *Materials* **2021**, *14*, 4225–4235.
6. Li, J.H.; Cai, Y.F.; Wu, H.M.; Yu, Z.A.; Yan, X.Z.; Zhang, Q.H.; Gao, T.Z.; Liu, K.; Jia, X.D.; Bao, Z.N. Polymers in Lithium-Ion and Lithium Metal Batteries. *Adv. Energy Mater.* **2021**, *11*, 2003239.
7. Wang, J.R.; Li, S.Q.; Zhao, Q.; Song, C.S.; Xue, Z.G. Structure Code for Advanced Polymer Electrolyte in Lithium-Ion Batteries. *Adv. Funct. Mater.* **2020**, *31*, 2008208.
8. Long, L.Z.; Wang, S.J.; Xiao, M.; Meng, Y.Z. Polymer Electrolytes for Lithium Polymer Batteries. *J. Mater. Chem. A* **2016**, *4*, 10038–10069.
9. Xue, Z.G.; He, D.; Xie, X.L. Poly(ethylene oxide)-Based Electrolytes for Lithium-Ion Batteries. *J. Mater. Chem. A* **2015**, *3*, 19218–19253.
10. Mindemark, J.; Lacey, M.J.; Bowden, T.; Brandell, D. Beyond PEO—Alternative Host Materials for Li⁺-Conducting Solid Polymer Electrolytes. *Prog. Polym. Sci.* **2018**, *81*, 114–143.
11. Fenton, D.E.; Parker, J.M.; Wright, P.V. Complexes of Alkali Metal Ions with Poly(ethylene oxide). *Polymer* **1973**, *14*, 589.
12. Yang, L.Y.; Wang, Z.J.; Feng, Y.C.; Tan, R.; Zuo, Y.X.; Gao, R.T.; Zhao, Y.; Han, L.; Wang, Z.Q.; Pan, F. Flexible Composite Solid Electrolyte Facilitating Highly Stable “Soft Contacting” Li-Electrolyte Interface for Solid State Lithium-Ion Batteries. *Adv. Energy Mater.* **2017**, *7*, 1701437.
13. Wei, Z.Y.; Chen, S.J.; Wang, J.Y.; Wang, Z.H.; Zhang, Z.H.; Yao, X.Y.; Deng, Y.H.; Xu, X.X. Superior Lithium Ion Conduction of Polymer Electrolyte with Comb-Like Structure Via Solvent-Free Copolymerization for Bipolar All-Solid-State Lithium Battery. *J. Mater. Chem. A* **2018**, *6*, 13438–13447.
14. Sun, Y.X.; Zhang, X.R.; Ma, C.H.; Guo, N.; Liu, Y.L.; Liu, J.; Xie, H.M. Fluorine-Containing Triblock Copolymers as Solid-State Polymer Electrolytes for Lithium Metal Batteries. *J. Power Sources* **2021**, *516*, 230686.
15. Bates, C.M.; Bates, F.S. 50th Anniversary Perspective: Block Polymers—Pure Potential. *Macromolecules* **2016**, *50*, 3–22.
16. Orilall, M.C.; Wiesner, U. Block Copolymer Based Composition and Morphology Control in Nanostructured Hybrid Materials for Energy Conversion and Storage: Solar Cells, Batteries, and Fuel Cells. *Chem. Soc. Rev.* **2011**, *40*, 520–535.
17. Xue, F.F.; Jiang, S.C. Elements of Functional Ion/Block Copolymer Hybrids. *RSC Adv.* **2013**, *3*, 23895.
18. Young, W.S.; Kuan, W.F.; Epps, T.H. Block Copolymer Electrolytes for Rechargeable Lithium Batteries. *J. Polym. Sci. Part B Polym. Phys.* **2014**, *52*, 1–16.
19. Wang, R.Y.; Park, M.J. Self-Assembly of Block Copolymers with Tailored Functionality: From the Perspective of Intermolecular Interactions. *Annu. Rev. Mater. Res.* **2020**, *50*, 521–549.

20. Zhai, L.; Chai, S.C.; Wang, G.; Zhang, W.; He, H.B.; Li, H.L. Triblock Copolymer/Polyoxometalate Nanocomposite Electrolytes with Inverse Hexagonal Cylindrical Nanostructures. *Macromol. Rapid Commun.* **2020**, *41*, 2000438.
21. Young, W.S.; Epps, T.H. Ionic Conductivities of Block Copolymer Electrolytes with Various Conducting Pathways: Sample Preparation and Processing Considerations. *Macromolecules* **2012**, *45*, 4689–4697.
22. Jung, H.Y.; Mandal, P.; Jo, G.; Kim, O.; Kim, M.; Kwak, K.; Park, M.J. Modulating Ion Transport and Self-Assembly of Polymer Electrolytes Via End-Group Chemistry. *Macromolecules* **2017**, *50*, 3224–3233.
23. Mizuno, H.; Hashimoto, K.; Tamate, R.; Kokubo, H.; Ueno, K.; Li, X.; Watanabe, M. Microphase-Separated Structures of Ion Gels Consisting of ABA-type Block Copolymers and an Ionic Liquid: A Key to Escape from the Trade-Off between Mechanical and Transport Properties. *Polymer* **2020**, *206*, 122849.
24. Chintapalli, M.; Le, T.N.P.; Venkatesan, N.R.; Mackay, N.G.; Rojas, A.A.; Thelen, J.L.; Chen, X.C.; Devaux, D.; Balsara, N.P. Structure and Ionic Conductivity of Polystyrene-*block*-poly(ethylene oxide) Electrolytes in the High Salt Concentration Limit. *Macromolecules* **2016**, *49*, 1770–1780.
25. Zhu, J.; Zhang, Z.; Zhao, S.; Westover, A.S.; Belharouak, I.; Cao, P.F. Single-Ion Conducting Polymer Electrolytes for Solid-State Lithium–Metal Batteries: Design, Performance, and Challenges. *Adv. Energy Mater.* **2021**, *11*, 2003836.
26. Lingua, G.; Grysan, P.; Vlasov, P.S.; Verge, P.; Shaplov, A.S.; Gerbaldi, C. Unique Carbonate-Based Single Ion Conducting Block Copolymers Enabling High-Voltage, All-Solid-State Lithium Metal Batteries. *Macromolecules* **2021**, *54*, 6911–6924.
27. Porcarelli, L.; Shaplov, A.S.; Salsamendi, M.; Nair, J.R.; Vygodskii, Y.S.; Mecerreyes, D.; Gerbaldi, C. Single-Ion Block Copoly(ionic liquid)s as Electrolytes for All-Solid State Lithium Batteries. *ACS Appl. Mater. Interfaces* **2016**, *8*, 10350–10359.
28. Feng, S.W.; Shi, D.Y.; Liu, F.; Zheng, L.P.; Nie, J.; Feng, W.F.; Huang, X.J.; Armand, M.; Zhou, Z.B. Single Lithium-Ion Conducting Polymer Electrolytes Based on Poly[(4-Styrenesulfonyl)(Trifluoromethanesulfonyl)Imide] Anions. *Electrochim. Acta* **2013**, *93*, 254–263.
29. Plechkova, N.V.; Seddon, K.R. Applications of Ionic Liquids in the Chemical Industry. *Chem. Soc. Rev.* **2008**, *37*, 123–150.
30. Han, J.H.; Lee, J.Y.; Suh, D.H.; Hong, Y.T.; Kim, T.H. Electrode-Impregnable and Cross-Linkable Poly(ethylene oxide)-Poly(Propylene Oxide)-Poly(ethylene oxide) Triblock Polymer Electrolytes with High Ionic Conductivity and a Large Voltage Window for Flexible Solid-State Supercapacitors. *ACS Appl. Mater. Interfaces* **2017**, *9*, 33913–33924.
31. Metwalli, E.; Kaepfel, M.V.; Schaper, S.J.; Kriele, A.; Gilles, R.; Raftopoulos, K.N.; Müller-Buschbaum, P. Conductivity and Morphology Correlations of Ionic-Liquid/Lithium-Salt/Block Copolymer Nanostructured Hybrid Electrolytes. *ACS Appl. Energy Mater.* **2018**, *1*, 666–675.
32. Zhang, R.S.; Chen, Y.F.; Montazami, R. Ionic Liquid-Doped Gel Polymer Electrolyte for Flexible Lithium-Ion Polymer Batteries. *Materials* **2015**, *8*, 2735–2748.
33. Wu, F.; Luo, L.F.; Tang, Z.H.; Liu, D.; Shen, Z.H.; Fan, X.H. Block Copolymer Electrolytes with Excellent Properties in a Wide Temperature Range. *ACS Appl. Energy Mater.* **2020**, *3*, 6536–6543.
34. Kitazawa, Y.; Iwata, K.; Imaizumi, S.; Ahn, H.; Kim, S.Y.; Ueno, K.; Park, M.J.; Watanabe, M. Gelation of Solvate Ionic Liquid by Self-Assembly of Block Copolymer and Characterization as Polymer Electrolyte. *Macromolecules* **2014**, *47*, 6009–6016.
35. Huang, J.; Wang, R.Y.; Tong, Z.Z.; Xu, J.T.; Fan, Z.Q. Influence of Ionic Species on the Microphase Separation Behavior of PCL-*b*-PEO/Salt Hybrids. *Macromolecules* **2014**, *47*, 8359–8367.
36. Zhang, Z.K.; Ding, S.P.; Zhou, Y.T.; Ye, Z.; Wang, R.Y.; Du, B.Y.; Xu, J.T. Influence of Salt Doping on the Entropy-Driven Lower Disorder-to-Order Transition Behavior of Poly(ethylene oxide-*b*-Poly(4-vinylpyridine)). *Macromol. Chem. Phys.* **2021**, *222*, 2100303.
37. Cao, X.H.; Yang, J.L.; Wang, R.Y.; Zhang, X.H.; Xu, J.T. Microphase Separation of Poly(propylene monothiocarbonate)-*b*-poly(ethylene oxide) Block Copolymers Induced by Differential Interactions with Salt. *Polymer* **2019**, *180*, 121745.
38. Cao, X.H.; Li, J.H.; Yang, M.J.; Yang, J.L.; Wang, R.Y.; Zhang, X.H.; Xu, J.T. Simultaneous Improvement of Ionic Conductivity and Mechanical Strength in Block Copolymer Electrolytes with Double Conductive Nanophases. *Macromol. Rapid Commun.* **2020**, *41*, 1900622.
39. Qian, W.J.; Texter, J.; Yan, F. Frontiers in Poly(ionic liquid)s: Syntheses and Applications. *Chem. Soc. Rev.* **2017**, *46*, 1124–1159.
40. Zhang, Z.J.; Zhang, Y.L.; Du, B.Y.; Peng, Z.Q. Liquid-Like Poly(Ionic Liquid) as Electrolyte for Thermally Stable Lithium-Ion Battery. *ACS Omega* **2018**, *3*, 10564–10571.
41. Wang, X.J.; Goswami, M.; Kumar, R.; Sumpter, B.G.; Mays, J. Morphologies of Block Copolymers Composed of Charged and Neutral Blocks. *Soft Matter* **2012**, *8*, 3036–3052.
42. Choi, J.H.; Ye, Y.S.; Elabd, Y.A.; Winey, K.I. Network Structure and Strong Microphase Separation for High Ion Conductivity in Polymerized Ionic Liquid Block Copolymers. *Macromolecules* **2013**, *46*, 5290–5300.
43. Zhang, Z.; Nasrabadi, A.T.; Aryal, D.; Ganesan, V. Mechanisms of Ion Transport in Lithium Salt-Doped Polymeric Ionic Liquid Electrolytes. *Macromolecules* **2020**, *53*, 6995–7008.
44. Wang, X.E.; Chen, F.F.; Girard, G.M.A.; Zhu, H.J.; MacFarlane, D.R.; Mecerreyes, D.; Armand, M.; Howlett, P.C.; Forsyth, M. Poly(ionic liquid)s-in-Salt Electrolytes with Co-Coordination-Assisted Lithium-Ion Transport for Safe Batteries. *Joule* **2019**, *3*, 2687–2702.
45. Zhou, N.; Wang, Y.F.; Zhou, Y.; Shen, J.Y.; Zhou, Y.; Yang, Y. Star-Shaped Multi-Arm Polymeric Ionic Liquid Based on Tetraalkylammonium Cation as High Performance Gel Electrolyte for Lithium Metal Batteries. *Electrochim. Acta* **2019**, *301*, 284–293.

46. Zhou, Y.; Wang, B.; Yang, Y.; Li, R.; Wang, Y.; Zhou, N.; Shen, J.; Zhou, Y. Dicationic Tetraalkylammonium-Based Polymeric Ionic Liquid with Star and Four-Arm Topologies as Advanced Solid-State Electrolyte for Lithium Metal Battery. *React. Funct. Polym.* **2019**, *145*, 104375.
47. Sharon, D.; Bennington, P.; Webb, M.A.; Deng, C.; de Pablo, J.J.; Patel, S.N.; Nealey, P.F. Molecular Level Differences in Ionic Solvation and Transport Behavior in Ethylene Oxide-Based Homopolymer and Block Copolymer Electrolytes. *J. Am. Chem. Soc.* **2021**, *143*, 3180–3190.
48. Young, W.S.; Albert, J.N.L.; Schantz, A.B.; Epps, T.H. Mixed-Salt Effects on the Ionic Conductivity of Lithium-Doped PEO-Containing Block Copolymers. *Macromolecules* **2011**, *44*, 8116–8123.
49. Lascaud, S.; Perrier, M.; Vallee, A.; Besner, S.; Prud'homme, J.; Armand, M. Phase Diagrams and Conductivity Behavior of Poly(ethylene oxide)-Molten Salt Rubbery Electrolytes. *Macromolecules* **1994**, *27*, 7469–7477.
50. Yoshizawa-Fujita, M.; Ishii, J.; Takeoka, Y.; Rikukawa, M. Oligoether/Zwitterion Diblock Copolymers: Synthesis and Application as Cathode-Coating Material for Li Batteries. *Polymers* **2021**, *13*, 800–812.
51. Niitani, T.; Shimada, M.; Kawamura, K.; Dokko, K.; Rho, Y.H.; Kanamura, K. Synthesis of Li⁺ Ion Conductive PEO-PSt Block Copolymer Electrolyte with Microphase Separation Structure. *Electrochem. Solid-State Lett.* **2005**, *8*, 385–388.
52. Bouchet, R.; Phan, T.N.T.; Beaudoin, E.; Devaux, D.; Davidson, P.; Bertin, D.; Denoyel, R. Charge Transport in Nanostructured PS-PEO-PS Triblock Copolymer Electrolytes. *Macromolecules* **2014**, *47*, 2659–2665.
53. Zhang, B.H.; Zhang, Y.H.; Zhang, N.; Liu, J.; Cong, L.; Liu, J.; Sun, L.Q.; Mager, A.; Julien, C.M.; Xie, H.M.; et al. Synthesis and Interface Stability of Polystyrene-Poly(ethylene glycol)-Polystyrene Triblock Copolymer as Solid-State Electrolyte for Lithium-Metal Batteries. *J. Power Sources* **2019**, *428*, 93–104.
54. Diederichsen, K.M.; Buss, H.G.; McCloskey, B.D. The Compensation Effect in the Vogel–Tammann–Fulcher (VTF) Equation for Polymer-Based Electrolytes. *Macromolecules* **2017**, *50*, 3831–3840.
55. Butzelaar, A.J.; Roring, P.; Mach, T.P.; Hoffmann, M.; Jeschull, F.; Wilhelm, M.; Winter, M.; Brunklaus, G.; Theato, P. Styrene-Based Poly(ethylene oxide) Side-Chain Block Copolymers as Solid Polymer Electrolytes for High-Voltage Lithium-Metal Batteries. *ACS Appl. Mater. Interfaces* **2021**, *13*, 39257–39270.
56. Butzelaar, A.J.; Roring, P.; Hoffmann, M.; Atik, J.; Paillard, E.; Wilhelm, M.; Winter, M.; Brunklaus, G.; Theato, P. Advanced Block Copolymer Design for Polymer Electrolytes: Prospects of Microphase Separation. *Macromolecules* **2021**, *54*, 11101–11112.
57. Rosenbach, D.; Mödl, N.; Hahn, M.; Petry, J.; Danzer, M.A.; Thelakkat, M. Synthesis and Comparative Studies of Solvent-Free Brush Polymer Electrolytes for Lithium Batteries. *ACS Appl. Energy Mater.* **2019**, *2*, 3373–3388.
58. Zhang, Q.H.; Huang, H.; Liu, T.M.; Wang, Y.; Yu, J.R.; Hu, Z.M. Molecular Composite Electrolytes of Polybenzimidazole/Polyethylene oxide with Enhanced Safety and Comprehensive Performance for All-Solid-State Lithium Ion Batteries. *Polymer* **2022**, *239*, 124450.
59. Wang, S.; Zhang, L.; Zeng, Q.H.; Liu, X.; Lai, W.Y.; Zhang, L.Y. Cellulose Microcrystals with Brush-Like Architectures as Flexible All-Solid-State Polymer Electrolyte for Lithium-Ion Battery. *ACS Sustain. Chem. Eng.* **2020**, *8*, 3200–3207.
60. Wu, F.; Wen, Z.Y.; Zhao, Z.K.; Bi, J.Y.; Shang, Y.X.; Liang, Y.H.; Li, L.; Chen, N.; Li, Y.J.; Chen, R.J. Double-Network Composite Solid Electrolyte with Stable Interface for Dendrite-Free Li Metal Anode. *Energy Storage Mater.* **2021**, *38*, 447–453.
61. Zhang, Z.K.; Ding, S.P.; Ye, Z.; Xia, D.L.; Xu, J.T. Thermodynamic Understanding the Phase Behavior of Fully Quaternized Poly(ethylene oxide)-B-Poly(4-Vinylpyridine) Block Copolymers. *Polymer* **2022**, *254*, 125045.